

# Real Singlet Scalar Benchmarks in the Multi-TeV Resonance Regime

Ian M. Lewis,<sup>1,\*</sup> Jacob Scott,<sup>1,†</sup> Miguel A. Soto Alcaraz,<sup>1,‡</sup> and Matthew Sullivan<sup>2,§</sup>

<sup>1</sup>*Department of Physics and Astronomy,  
University of Kansas, Lawrence, Kansas, 66045 U.S.A.*

<sup>2</sup>*High Energy Theory Group, Physics Department,  
Brookhaven National Laboratory, Upton, New York, 11973 U.S.A.*

## Abstract

Scalar extensions of the Standard Model are of much interest at the LHC and future colliders. In particular, these models can give rise to resonant di-Higgs production and alter the Higgs trilinear coupling. In this paper, we study di-Higgs production in the Standard Model extended by a real scalar singlet with no additional symmetries. We determine how large the resonant di-Higgs rate and variation in the Higgs trilinear coupling can be in four scenarios: current LHC results and projected results at the HL-LHC, the HL-LHC combined with a circular  $e^-e^+$  collider such as the CEPC or FCC-ee, and the HL-LHC combined with a linear  $e^-e^+$  collider such as the ILC. While these are updated results from a previous study [1] using current LHC data, we go further and find benchmark points in the multi-TeV resonance regime for future colliders beyond the HL-LHC. Considering current LHC results, the resonant di-Higgs rate can still be an order of magnitude larger than the SM predicted di-Higgs rate. In the HL-LHC scenario, the Higgs trilinear coupling can still be a factor of three larger than the SM prediction for resonance masses in the 1.5–3.5 TeV range, where resonant searches may have less reach. This enhancement is just at the projected  $2\sigma$  sensitivity of the HL-LHC. We find there are resonance masses for which the change in the Higgs trilinear is maximized while the resonant rate is negligible. We provide an analytical understanding of these effects with a discussion on the interplay of various constraints on the parameter space and the Higgs trilinear coupling.

---

\*Electronic address: ian.lewis@ku.edu

†Electronic address: jacob.scott@ku.edu

‡Electronic address: msoto1@ku.edu

§Electronic address: msullivan1@bnl.gov

## I. INTRODUCTION

Measurements of the observed Higgs boson properties are some of the major long term goals of the Large Hadron Collider (LHC) and future colliders [2, 3]. Of particular interest is the measurement of the Higgs potential [4], which is the source of electroweak symmetry breaking (EWSB) within the Standard Model (SM). So far only the quadratic term in the potential has been directly measured via the Higgs mass. The most promising route to further directly measure the shape of the potential is to measure the cubic term via the Higgs trilinear coupling and di-Higgs production. The LHC is projected to limit the trilinear coupling to be between zero and 2.7 times the SM value at the  $2\sigma$  level [5]. Hence, models that alter the di-Higgs rate are of much interest [4].

In this paper we study di-Higgs production in the simplest extension of the SM: the addition of a real gauge singlet scalar with no additional symmetries. This model and signal has been much studied in the literature with and without an additional  $Z_2$  symmetry on the new scalar [1, 6–32]. The real singlet scalar only couples to the SM via the scalar potential at the renormalizable level<sup>1</sup>. Since the shape of the Higgs potential is changed, this model can help provide a strong first order electroweak (EW) phase transition necessary for EW baryogenesis [29–43]. That is, it is a well-motivated model that introduces interesting new physics related to the Higgs sector. Hence, the real singlet scalar model is a good benchmark model for the LHC and future colliders.

The main results of this paper are finding the maximum allowed resonant di-Higgs rates and variation in the Higgs trilinear coupling in this model. This is an update on previous results [1] to take into account current LHC bounds [44], as well as extending that work to provide benchmarks assuming various future collider possibilities. In addition to the high luminosity LHC (HL-LHC), we consider several different scenarios with precision electron-positron colliders. For example, there are the possibilities of linear electron-positron colliders such as the International Linear Collider (ILC) [45–47], or circular electron-positron colliders such as the CEPC [48, 49] or FCC-ee [50]. We consider four scenarios [44]:

- S1: Current LHC constraints from precision Higgs measurements and scalar

---

<sup>1</sup> Non-renormalizable interaction can introduce new couplings between the singlet scalar and gauge bosons and fermions that affect interpretations of the simplest model [24].

searches [44].

- S2: Projections for Higgs precision measurements and scalar searches at the HL-LHC [2, 3].
- S3: Projections for Higgs precision measurements and scalar searches at the HL-LHC and the CEPC or FCC-ee (HL-LHC+FCCee) [2, 3]
- S4: Projections for Higgs precision measurements and scalar searches at the HL-LHC and a 500 GeV ILC (HL-LHC+ILC500) [2, 3].

Scenario S1 is the update on Ref. [1] and provides benchmark points for the LHC and the HL-LHC. Scenarios S2-S4 project benchmark points for future high energy colliders up to resonance masses of 10 TeV. The results for scenarios S2-S4 are presented in such a way as to be relevant for most future high energy collider possibilities, including the HL-LHC, 100 TeV pp colliders [51–53] or a future muon collider [54–57]. We find that there can still be significant enhancements in the Higgs trilinear coupling in the TeV to multi-TeV range, up to a factor of three larger than the SM predictions. Such resonances may be out of the reach of the LHC, and a variation in the Higgs trilinear may be the first indication of new physics.

In Sec. II we provide a description of the model. Various theoretical and experimental constraints are presented in Sec. III. The results for the maximum di-Higgs rate as well as the allowed ranges for the Higgs trilinear couplings in scenarios S1-S4 are given in Sec. IV. We conclude in Sec. V.

## II. HIGGS SINGLET MODEL

The model extends the SM by adding a real gauge singlet scalar  $S = x + s$ , where  $\langle S \rangle = x$  is the vacuum expectation value (vev) of  $S$ . This new singlet scalar can only couple directly to the SM at the renormalizable level via the scalar potential [13]:

$$\begin{aligned}
 V(\Phi, S) = & -\mu^2 \Phi^\dagger \Phi + \lambda (\Phi^\dagger \Phi)^2 + \frac{a_1}{2} \Phi^\dagger \Phi S + \frac{a_2}{2} \Phi^\dagger \Phi S^2 \\
 & + b_1 S + \frac{b_2}{2} S^2 + \frac{b_3}{3} S^3 + \frac{b_4}{4} S^4,
 \end{aligned}
 \tag{1}$$

where

$$\Phi = \frac{1}{\sqrt{2}} \begin{pmatrix} \sqrt{2}G^+ \\ v + h + iG^0 \end{pmatrix} \quad (2)$$

is the Higgs doublet,  $v$  is the SM Higgs vev,  $h$  is the SM Higgs boson, and  $G^+, G^0$  are the Goldstone bosons.

Shifting the field  $S$  by a constant value  $S \rightarrow S + \delta S$  is simply a redefinition of parameters with no physical consequence [13]. Additionally, the singlet vev cannot contribute to gauge boson or fermion masses. Hence, we can choose  $(v, x) = (v_{\text{EW}}, 0)$ , with  $v_{\text{EW}} = 246$  GeV, to be the EW symmetry breaking minimum that recreates the SM mass spectrum. The requirement that this is a minimum of the potential yields

$$\mu^2 = \lambda v_{\text{EW}}^2 \quad \text{and} \quad b_1 = -\frac{v_{\text{EW}}^2}{4}a_1. \quad (3)$$

After EWSB, there are two scalar mass eigenstates  $h_1$  and  $h_2$  with masses  $m_1$  and  $m_2$ , respectively, that are admixtures of the scalar bosons  $h$  and  $s$ :

$$\begin{pmatrix} h_1 \\ h_2 \end{pmatrix} = \begin{pmatrix} \cos \theta & \sin \theta \\ -\sin \theta & \cos \theta \end{pmatrix} \begin{pmatrix} h \\ s \end{pmatrix}. \quad (4)$$

Throughout the rest of the paper we will assume  $h_1$  is the observed Higgs boson with  $m_1 = 125$  GeV [58] and  $h_2$  is a heavier new scalar ( $m_2 > 2m_1$ ). Several parameters in the potential can be replaced with the masses  $m_1, m_2$  and the scalar mixing angle  $\theta$  [13]:

$$a_1 = \frac{m_1^2 - m_2^2}{v_{\text{EW}}} \sin 2\theta, \quad (5)$$

$$b_2 = m_1^2 \sin^2 \theta + m_2^2 \cos^2 \theta - \frac{a_2 v_{\text{EW}}^2}{2}, \quad (6)$$

$$\lambda = \frac{m_1^2 \cos^2 \theta + m_2^2 \sin^2 \theta}{2v_{\text{EW}}^2}. \quad (7)$$

Including vevs, masses, and mixing angle, the only other free parameters are  $a_2$ ,  $b_3$ , and  $b_4$ .

After symmetry breaking, the scalar mass eigenstates have the cubic self-interactions

$$V \supset \frac{\lambda_{111}}{3!} h_1^3 + \frac{\lambda_{112}}{2!} h_2 h_1^2 + \frac{\lambda_{122}}{2!} h_2^2 h_1 + \frac{\lambda_{222}}{3!} h_2^3. \quad (8)$$

The results for the trilinear couplings can be found in Ref. [13]. For di-Higgs production, the relevant trilinear couplings are  $\lambda_{111}$  and  $\lambda_{112}$ . The former can affect the di-Higgs rate

through non-resonant  $h_1$  production,  $pp \rightarrow h_1^* \rightarrow h_1 h_1$ , and the latter through resonant  $h_2$  production,  $pp \rightarrow h_2 \rightarrow h_1 h_1$ . The partial width for  $h_2 \rightarrow h_1 h_1$  is

$$\Gamma(h_2 \rightarrow h_1 h_1) = \frac{\lambda_{112}^2}{32\pi m_2} \sqrt{1 - \frac{4m_1^2}{m_2^2}}. \quad (9)$$

For completeness, the relevant trilinears for  $h_1 h_1$  production [13] are

$$\lambda_{111} = 3 \frac{m_1^2}{v_{\text{EW}}} \cos^3 \theta + 2 b_3 \sin^3 \theta + 3 a_2 v_{\text{EW}} \cos \theta \sin^2 \theta, \quad (10)$$

$$\lambda_{112} = \sin \theta \left[ -\frac{2m_1^2 + m_2^2}{v_{\text{EW}}} \cos^2 \theta + 2a_2 v_{\text{EW}} \left( 1 - \frac{3}{2} \sin^2 \theta \right) + b_3 \sin 2\theta \right]. \quad (11)$$

### III. CONSTRAINTS

The real singlet scalar model is subject to various theoretical and experimental constraints. In this section, we give an overview of the constraints that we impose to determine the maximum di-Higgs rates and variations in the trilinear Higgs coupling.

#### A. Vacuum Stability and Perturbative Unitarity

The quartic couplings in the scalar potential are bounded by two conditions: vacuum stability and perturbative unitarity. For the theory to be viable, the scalar potential needs to be bounded from below so that it does not decay in a runaway direction. That is, it should be positive at large field values:

$$\frac{\lambda}{4} h^4 + \frac{a_2}{4} h^2 s^2 + \frac{b_4}{4} s^4 > 0. \quad (12)$$

Stability along the axes  $s = 0$  and  $h = 0$  implies that both  $\lambda$  and  $b_4$  are positive. Additionally, if  $a_2$  is positive, the potential is bounded from below. However,  $a_2$  can also be negative. To see this, rewrite the quartic terms as

$$\frac{\lambda}{4} \left( h^2 + \frac{a_2 s^2}{2\lambda} \right)^2 + \frac{1}{4} \left( b_4 - \frac{a_2^2}{4\lambda} \right) s^4. \quad (13)$$

The potential is stable for

$$a_2 \geq -2\sqrt{\lambda b_4}. \quad (14)$$

To maintain a perturbative theory, we will also impose perturbative unitarity. Following from scattering theory applied to QFT, the matrix element of any two-to-two scalar

scattering can be written in terms of the Legendre polynomials as

$$\mathcal{M} = 16\pi \sum_k (2k+1) a_k P_k(\cos \theta), \quad (15)$$

where  $a_k$  are complex parameters. The unitarity bound from the outgoing and incoming waves implies that  $a_k$  lies within a circle of radius  $1/2$  centered at  $i/2$ . This leads to the typical perturbative unitarity constraints

$$|\text{Re}(a_k)| \leq 1/2. \quad (16)$$

This constraint is usually applied at tree level, where saturation of the limit implies that there is at minimum a 41% higher order correction to the scattering processes [59]. At high energies the matrix elements for two-to-two scalar scattering are

$$a_0 = \frac{3b_4}{8\pi} \quad \text{for } ss \rightarrow ss, \quad (17)$$

$$a_0 = \frac{a_2}{16\pi} \quad \text{for } sh \rightarrow sh, \text{ and} \quad (18)$$

$$a_0 = \frac{3\lambda}{8\pi} \quad \text{for } hh \rightarrow hh. \quad (19)$$

While perturbative unitarity places upper and lower bounds on the quartic couplings, the lower bounds from vacuum stability are more constraining. The perturbative unitarity and vacuum stability bounds on the quartic couplings are then

$$0 \leq b_4 \leq \frac{4\pi}{3}, \quad 0 \leq \lambda \leq \frac{4\pi}{3}, \quad \text{and} \quad -2\sqrt{\lambda b_4} \leq a_2 \leq 8\pi. \quad (20)$$

## B. Global Minimization

The scalar potential in Eq. (1) has six possible extrema, with one minimum at  $(v, x) = (v_{\text{EW}}, 0)$  by construction. Since the singlet scalar does not contribute to gauge boson or fermion masses and the other minima do not correspond to a Higgs vev of  $v_{\text{EW}}$ , the global minimum of the scalar potential must be  $(v, x) = (v_{\text{EW}}, 0)$ . This constraint places meaningful bounds on  $a_2$  and  $b_3$ . These bounds are relevant for  $\lambda_{112}$  and  $pp \rightarrow h_2 \rightarrow h_1 h_1$  rates. For completeness, in Fig. 1 we show the allowed region for  $a_2$  and  $b_3$  under these constraints together with a heat map for  $\text{BR}(h_2 \rightarrow h_1 h_1)$  for two different choices of  $b_4$ . The branching ratio of  $h_2 \rightarrow h_1 h_1$  is maximized on the boundaries of the allowed space, but never reaches one. That is, theoretical constraints on the global minimum place meaningful bounds on how large  $\text{BR}(h_2 \rightarrow h_1 h_1)$  can be. Figure 1 reproduces the results in Refs. [1, 13], where more details can be found.

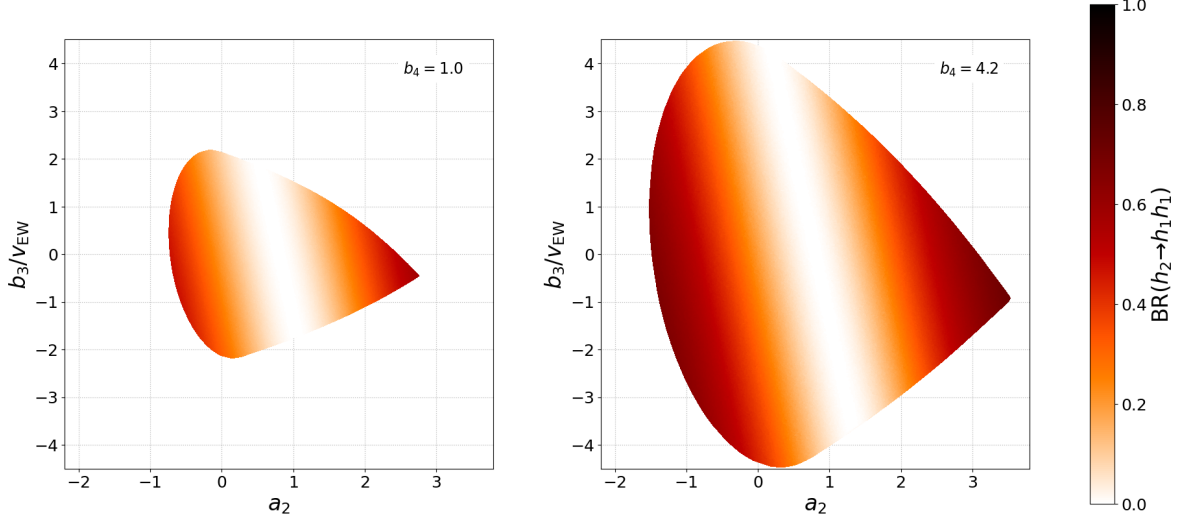


FIG. 1: Heat maps of  $\text{BR}(h_2 \rightarrow h_1 h_1)$  in the allowed  $b_3 - a_2$  plane for  $m_2 = 800$  GeV and  $\sin \theta = 0.14$ . In the left figure  $b_4 = 1.0$ , and in the right figure  $b_4 = 4.2$ .

### C. Experimental

The singlet model affects precision Higgs rates as well as providing new avenues for discovery via the production of the new scalar. Higgs precision measurements are typically quoted in terms of signal strengths

$$\mu_f^i = \frac{\sigma_i(pp \rightarrow h_1)}{\sigma_{i,\text{SM}}(pp \rightarrow h_1)} \frac{\text{BR}(h_1 \rightarrow f)}{\text{BR}_{\text{SM}}(h_1 \rightarrow f)}, \quad (21)$$

where the initial state is  $i$ , the final state  $f$ , and the subscript SM indicates SM values. In the renormalizable real singlet model with  $m_2 > m_1$ , from the mixing in Eq. (4), all production and decay rates for  $h_1$  are universally suppressed by  $\cos^2 \theta$  compared to the SM rates:

$$\sigma_i(pp \rightarrow h_1) = \cos^2 \theta \sigma_{i,\text{SM}}(pp \rightarrow h_1) \quad \text{and} \quad \Gamma(h_1 \rightarrow f) = \cos^2 \theta \Gamma_{\text{SM}}(h_1 \rightarrow f). \quad (22)$$

The branching ratios of  $h_1$  are unchanged from SM predictions since they are ratios of rates. Hence, there is a universal signal strength for all production and decay channels:

$$\mu_f^i = \cos^2 \theta. \quad (23)$$

That is, measurements of signal strengths will constrain  $\theta$  independently of the mass of  $h_2$ .

Meanwhile, the couplings of  $h_2$  to SM gauge bosons and fermions are suppressed by  $\sin \theta$  relative to the SM prediction for Higgs couplings. Hence, the production rates from and decay rates into SM gauge bosons and fermions are

$$\sigma_i(pp \rightarrow h_2) = \sin^2 \theta \sigma_{i,\text{SM}}(pp \rightarrow h_2) \quad \text{and} \quad \Gamma(h_2 \rightarrow f_{\text{SM}}) = \sin^2 \theta \Gamma_{\text{SM}}(h_2 \rightarrow f_{\text{SM}}), \quad (24)$$

where  $f_{\text{SM}}$  are final state SM gauge bosons or fermions, and the subscript SM refers to SM Higgs predictions at the mass of  $h_2$ . Above the di-Higgs threshold the new decay  $h_2 \rightarrow h_1 h_1$  opens up and the total width for  $h_2$  is given then by

$$\Gamma(h_2) = \Gamma(h_2 \rightarrow h_1 h_1) + \Gamma(h_2 \rightarrow f_{\text{SM}}). \quad (25)$$

The total rate is then approximated using the narrow width approximation

$$\sigma_i(pp \rightarrow h_2 \rightarrow f) \approx \sigma_i(pp \rightarrow h_2) \text{BR}(h_2 \rightarrow f). \quad (26)$$

To ensure that the narrow width approximation is valid, we demand that the total  $h_2$  width is less than 10% of its mass:

$$\Gamma(h_2) \leq 0.1 m_2. \quad (27)$$

Such a constraint also helps keep the theory perturbative.

In Fig. 2, we show the upper bounds on the scalar mixing angle  $|\sin \theta|$  for scenarios S1-S4 as described in the Introduction. For current LHC constraints from Higgs precision and direct scalar searches, we use the results of Ref. [44]. These constraints have two scenarios for combining precision Higgs measurements with scalar searches: a “hard cut” and “ $\Delta\chi^2$ ” method [24, 44, 60, 61]. We consider both results. For the HL-LHC, FCC-ee, and ILC500 we use the projections from the 2019 European Strategy Report [3] and Snowmass 2022 [2]. As discussed previously around Eq. (23), Higgs precision measurements constrain  $\sin \theta$  independent of the  $h_2$  mass. Hence, flat regions in Fig. 2 arise from fitting Higgs data. At masses around or below 1 TeV, scalar searches can dominate leading to a mass dependent  $\sin \theta$  bound. At the LHC scalar searches are always more constraining, while for the other scenarios Higgs precision can be more constraining.

The constraint from the narrow width is also shown as a shaded region in Fig. 2. At high masses, the decays  $h_2 \rightarrow W^\pm W^\mp$ ,  $h_2 \rightarrow ZZ$ , and  $h_2 \rightarrow h_1 h_1$  dominate. From the Goldstone Boson Equivalence Theorem, the total width of  $h_2$  is then

$$\Gamma(h_2) \approx \frac{4}{3} \sin^2 \theta \Gamma_{\text{SM}}(h_2) \approx \frac{m_2^3}{8 \pi v_{\text{EW}}^2} \sin^2 \theta. \quad (28)$$



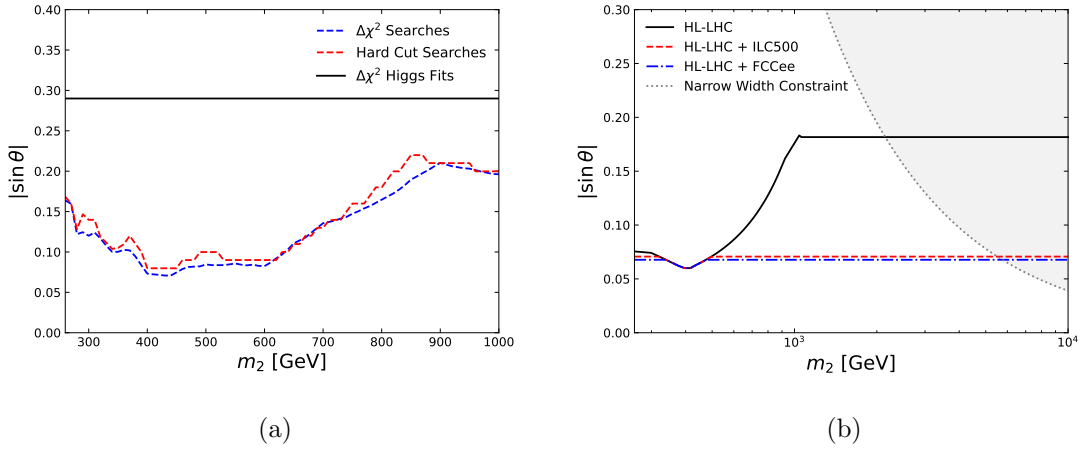


FIG. 2: (a) Mixing angle constraints for scenario S1 from (black solid) Higgs precision measurement, (red dashed) hard cut bounds from scalar searches, and (blue dashed) a  $\Delta\chi^2$  combination of scalar searches and Higgs precision measurements. (b) Mixing angle constraints for scenarios (black solid) S2, (blue dot dashed) S3, and (red dashed) S4. The shaded region is excluded by the narrow width requirement.

Equation (27) leads to a bound on  $\sin \theta$  of

$$\sin^2 \theta \lesssim \frac{0.8\pi v_{\text{EW}}^2}{m_2^2}. \quad (29)$$

This is a monotonically decreasing upper bound on  $\sin \theta$  for large  $m_2$ . The narrow width constraint is dominant over experimental limits for the HL-LHC when  $m_2 \gtrsim 2.1$  TeV and for HL-LHC+FCCee and HL-LHC+ILC500 when  $m_2 \gtrsim 5.7$  TeV.

#### IV. RESULTS

We now provide the main results of this paper: finding the maximum allowed resonant di-Higgs rate and Higgs trilinear couplings in the real singlet extension. As discussed in the Introduction, we consider four scenarios for experimental constraints from different colliders

- S1: Current LHC [44].
- S2: The HL-LHC [2, 3].
- S3: The HL-LHC+FCCee [2, 3].

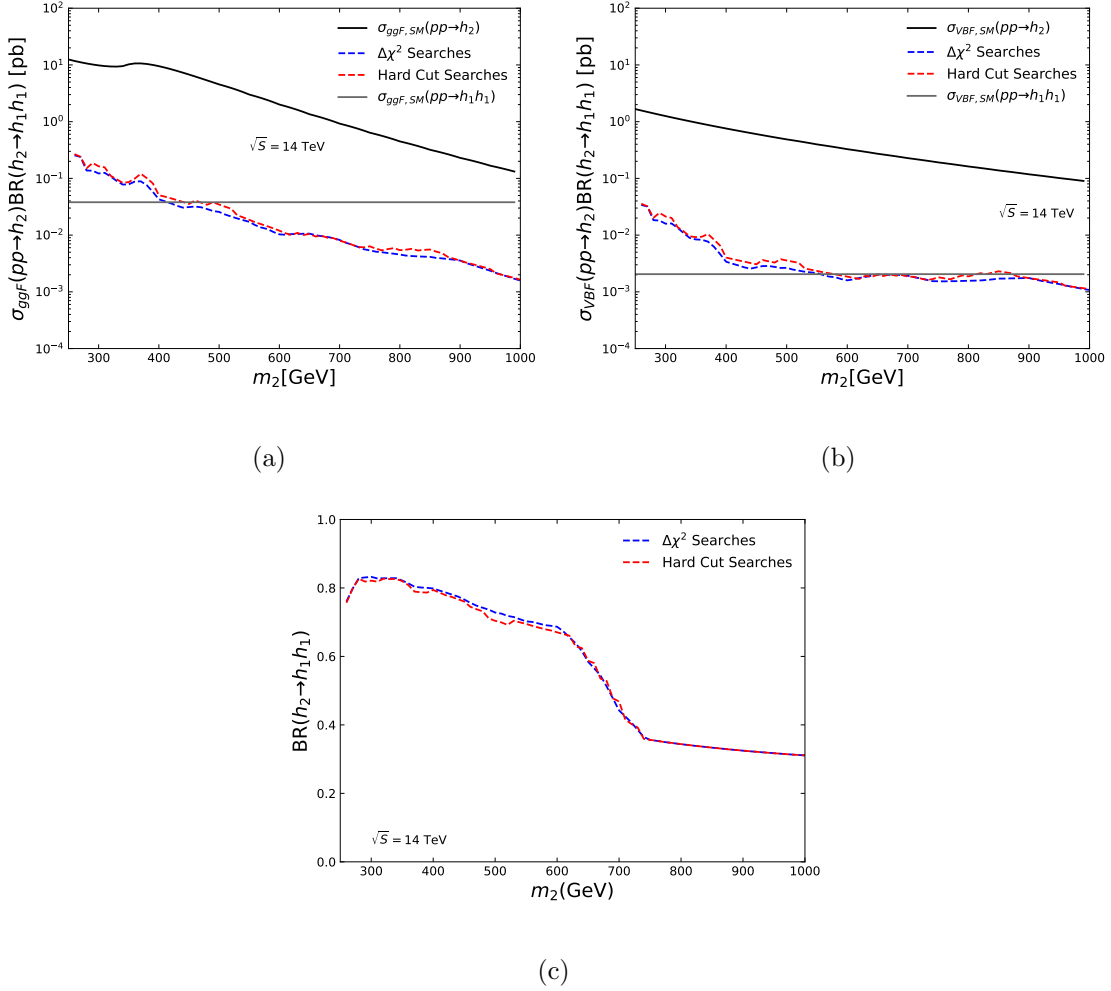


FIG. 3: Maximum allowed cross section  $\sigma(pp \rightarrow h_2 \rightarrow h_1 h_1)$  in scenario S1 at lab frame energy  $\sqrt{S} = 14$  TeV for (a) gluon fusion and (b) VBF, with (c) the corresponding branching ratio  $\text{BR}(h_2 \rightarrow h_1 h_1)$ . Two possibilities for  $\sin\theta$  limits from Higgs precision and scalar searches are shown: blue dashed lines for the  $\Delta\chi^2$  combination and red dashed for the hard cut limits. In (a,b) the light grey line is for the SM di-Higgs rate and the black solid the SM production rate at mass  $m_2$  for (a) gluon fusion and (b) VBF.

- S4: The HL-LHC+ILC500 [2, 3].

All constraints in Sec. III, including all theoretical constraints, are applied to a scan over  $\sin\theta$ ,  $a_2$ ,  $b_3$ ,  $b_4$ , and  $m_2$ .

In Fig. 3 we show the maximum allowed resonant di-Higgs rates in scenario S1 for the (a) gluon fusion and (b) vector boson fusion (VBF) production modes of  $h_2$  together with (c) the associated branching ratio  $\text{BR}(h_2 \rightarrow h_1 h_1)$ . The current LHC precision Higgs measurements

are combined with scalar searches using a traditional (red dashed) “hard cut” method [24, 44, 60, 61] as well as a (blue dashed) “ $\Delta\chi^2$ ” [24, 44] combination. As can be seen, both methods have very similar results. For comparison we have included the predicted SM rates for (black solid) a SM Higgs produced at mass  $m_2$  and the (grey solid) SM di-Higgs rates. As can be seen, at the di-Higgs threshold the gluon fusion rate can still be  $\sim 5 - 10$  times larger than SM di-Higgs, and the VBF rate can be  $\sim 15 - 20$  times larger. At larger masses near 1 TeV, the maximum gluon fusion rate is over an order of magnitude less than the SM di-Higgs rate while the maximum VBF rate is only a factor of two less than the SM rate. Although the  $\sin\theta$  limit does not change much between  $m_2 \sim 250 - 1000$  GeV, the SM cross section at  $m_2$  and the  $\text{BR}(h_2 \rightarrow h_1 h_1)$  do decrease with mass. The branching ratio of  $h_2 \rightarrow h_1 h_1$  corresponding to the maximum rate is near 80% near the di-Higgs threshold. However, as  $m_2$  increases,  $\text{BR}(h_2 \rightarrow h_1 h_1)$  decreases approaching 1/4 as dictated by the Goldstone Boson Equivalence Theorem.

Scenarios S2-S4 are projections for future colliders such as a 100 TeV pp collider [51–53]. Since it is unknown which future high energy colliders may be built, we present the results normalized to the SM prediction for the production of the SM Higgs boson at mass  $m_2$ :

$$\frac{\sigma(pp \rightarrow h_2 \rightarrow h_1 h_1)}{\sigma_{\text{SM}}(pp \rightarrow h_2)} \approx \sin^2 \theta \text{BR}(h_2 \rightarrow h_1 h_1). \quad (30)$$

These rates can then be translated to any collider in which  $h_2$  is singly produced via couplings to SM vector boson or fermions via renormalizable interactions.

In Fig. 4 the (a) normalized maximum resonant di-Higgs rate and (b) the corresponding branching ratios for scenarios S2-S4 are shown. For masses below 1 TeV, these projected maximum rates are compared to the current constraints on di-Higgs resonance rates in Fig. 4(c). As can be seen, the projected maximum rates are still below current constraints. Although, the current limit on resonant di-Higgs production is very close to the maximum rate for the HL-LHC projection at  $m_2 \sim 600$  GeV.

The projected maximum rates and corresponding branching ratios in these scenarios have some interesting behaviors. First, we discuss the HL-LHC results. The maximum rate decreases from  $m_2 \sim 275$  GeV to 425 GeV then starts increasing with the increasing  $|\sin\theta|$  limit in Fig. 2(b). Around  $m_2 \sim 750 - 820$  GeV, the projected maximum rate decreases and then increases again. For  $h_2$  masses near but below 500 GeV, the maximum  $\text{BR}(h_2 \rightarrow h_1 h_1)$  decreases more quickly than the bound on  $|\sin\theta|$  increases, causing the

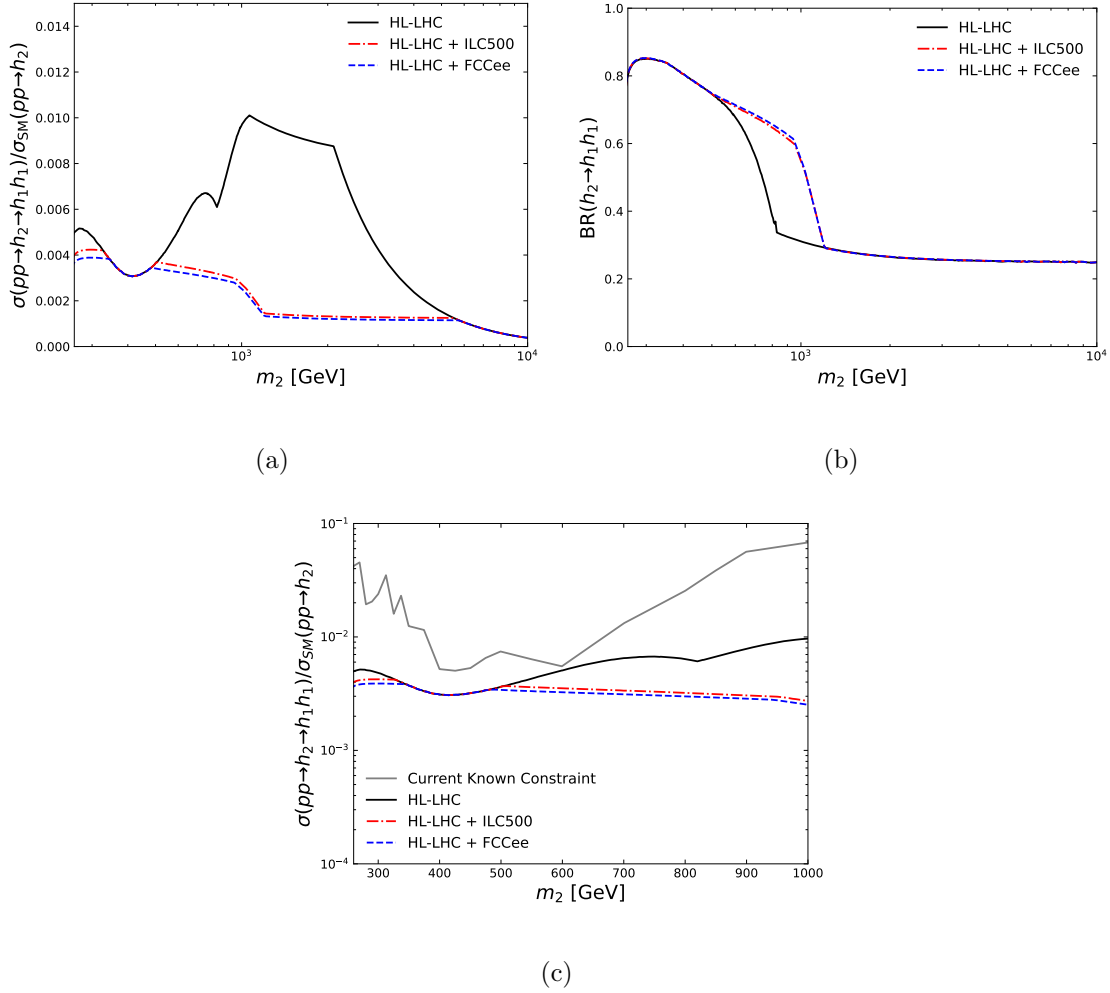


FIG. 4: (a) The normalized maximum double Higgs resonant production rates and (b) the corresponding branching ratio  $BR(h_2 \rightarrow h_1 h_1)$  for scenarios (black solid) S2, (blue dashed) S3, and (red dot-dashed) S4. In (c) the maximum rates are compared to (grey solid) current di-Higgs upper bounds.

maximum rate to decrease. Between 500 – 750 GeV, the bounds on  $\sin \theta$  increases more quickly than the decrease in branching ratio. At 750 GeV, the branching ratio of  $h_2 \rightarrow h_1 h_1$  drops precipitously causing a drop in the allowed maximum rate. Above  $m_2 \sim 820$  GeV, the change in the  $h_2 \rightarrow h_1 h_1$  branching ratio flattens. The maximum production rate then starts increasing quickly with  $|\sin \theta|$  until  $m_2 \sim 1.1$  TeV when the  $|\sin \theta|$  bound is from precision Higgs constraints and is flat. Between  $m_2 \sim 1.1 - 2.1$  TeV, the maximum rate decreases with the slow decrease in  $BR(h_2 \rightarrow h_1 h_1)$ . For masses  $m_2 \gtrsim 2.1$  TeV, the bound on  $|\sin \theta|$  decreases quickly due to the narrow width constraint as shown in Eq. (29). Hence,

the maximum rate also decreases quickly.

The behavior of the maximum rates and corresponding branching ratios for the future electron-positron collider scenarios HL-LHC+FCCee and HL-LHC+ILC500 are similar to HL-LHC, but with different mass scales. For masses up to  $m_2 \sim 1.2$  TeV, the total rate decreases due to a flat upper bound on  $|\sin \theta|$  and decreasing branching ratio. This behavior is only interrupted when the HL-LHC direct scalar search bounds are more constraining than the precision Higgs constraints for  $m_2 \sim 350 - 500$  GeV. Around  $m_2 \sim 1$  TeV the  $h_2 \rightarrow h_1 h_1$  branching ratio corresponding to the maximum rate drops quickly and then flattens out for  $m_2 \gtrsim 1.2$  TeV. Hence, between  $\sim 1.2$  TeV and 5.7 TeV the maximum rate is flat corresponding to a flat  $|\sin \theta|$  bound and mostly flat  $h_2 \rightarrow h_1 h_1$  branching ratio. Above 5.7 TeV, the narrow width constraint of Eq. (29) sets in, and the maximum rate decreases with the  $|\sin \theta|$  limit.

The maximum rate in all cases is continuous, although there are kinks. However, in scenarios S2-S4, the corresponding branching ratio for  $h_2 \rightarrow h_1 h_1$  and  $|\sin \theta|$  have some interesting behavior. There are clearly two different regions for the branching ratios: a slight increase above threshold with a decrease soon after, and then at  $m_2 \sim 800$  GeV for the HL-LHC and  $m_2 \sim 1.1 - 1.2$  TeV for HL-LHC+ILC500 and HL-LHC+FCCee, the branching ratios drops precipitously and then flattens out. This is particularly striking at the HL-LHC, where the branching ratio for  $h_2 \rightarrow h_1 h_1$  and  $|\sin \theta|$  (see Fig. 5(c)) have a discontinuity at  $m_2 \approx 800$  GeV.

To explain these effects, we will focus on the HL-LHC scenario, although the explanations for HL-ILC+ILC500 and HL-LHC+FCCee are similar. First, we explain why the branching ratio changes from steeply falling to nearly flat. From Fig. 1, the rate is maximized on the borders of the allowed parameter space. Which side of this space that the maximum rate occurs on depends on the precise mass  $m_2$  and scalar mixing angle. Transitioning from one side to the other changes the behavior  $\text{BR}(h_2 \rightarrow h_1 h_1)$  corresponding to the maximum rate. To see this more clearly, Fig. 5(a) shows the  $a_2, b_3$  corresponding to the maximum rate for  $m_2 = 800$  GeV. The change from one region of parameter space to the other occurs at  $|\sin \theta| \sim 0.14$ . For  $|\sin \theta| \gtrsim 0.14$  GeV, the parameter  $a_2$  is near zero. From Eq. (11), when  $a_2$  and  $\sin \theta$  are small the  $h_1 - h_1 - h_2$  coupling and  $\text{BR}(h_2 \rightarrow h_1 h_1)$  are largely independent of the model parameters  $a_2, b_3$ . Additionally, as shown in in Fig. 5(b), the rate does not monotonically increase as  $|\sin \theta|$  increases. Indeed, right below  $|\sin \theta| \approx 0.14$  the rate is

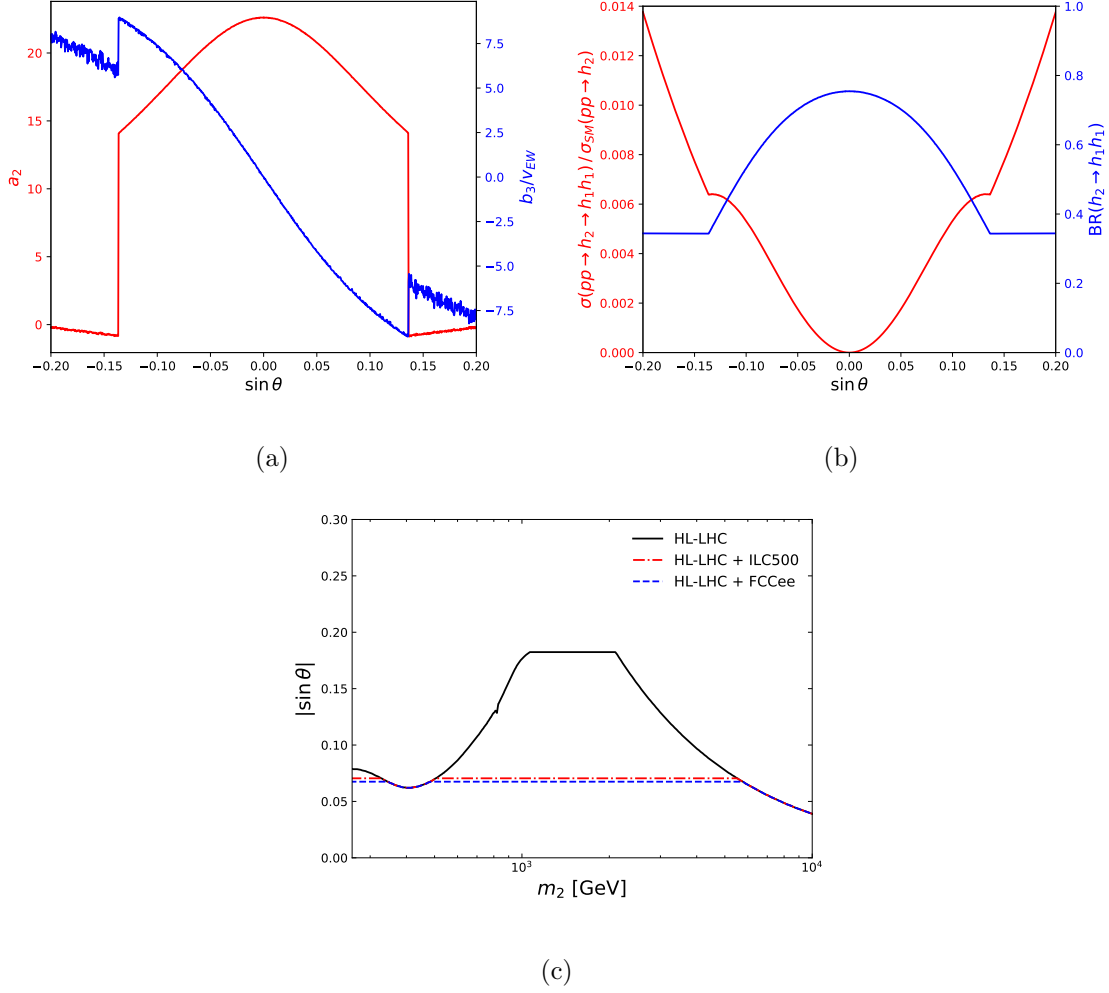


FIG. 5: (a) Values for (red)  $a_2$  and (blue)  $b_3/v_{EW}$  that maximize the double Higgs rate for  $m_2 = 800$  GeV as a function of mixing angle. (b) The (red) maximum double Higgs rate normalized to SM-like production cross section and (blue) the corresponding  $BR(h_2 \rightarrow h_1 h_1)$  as a function of  $\sin \theta$ . (c) The  $|\sin \theta|$  corresponding to the maximum resonant di-Higgs rate as a function of  $m_2$  for scenarios (black) S2, (blue dashed) S3, and (red dot-dashed) S4.

maximized.

For each mass  $m_2$  there is a  $|\sin \theta|$  ( $|\sin \theta_0|$ ) for which these two effects occur: the branching ratio flattens for  $|\sin \theta| \geq |\sin \theta_0|$  and there is a local maximum in the rate at a value of  $|\sin \theta|$  ( $|\sin \theta_{\max}|$ ) near but below  $|\sin \theta_0|$ . These effects are relevant when the experimental limits on  $|\sin \theta|$  and  $|\sin \theta_0|$  coincide, as long as the corresponding values of  $a_2, b_3$  are allowed within other constraints on the model. In Fig. 5(c), we show the  $|\sin \theta|$  corresponding to the maximum rate. For the HL-LHC scenario there is a discontinuity in

$|\sin \theta|$  at  $m_2 \sim 800$  GeV. This is precisely where  $|\sin \theta_0|$  and the experimental limits coincide. In principle, this effect also occurs for scenarios S3 and S4 with the lepton colliders. However, this would be at  $m_2 \sim 2$  TeV and in that case the corresponding  $a_2$  is far beyond the perturbative unitarity limit in Eq. (20). Hence, the  $|\sin \theta|$  corresponding to the maximum rates for the HL-LHC+FCCee and HL-LHC+ILC500 scenarios are exactly the maximum  $|\sin \theta|$  allowed in Fig. 2(b).

### A. Variation in the Higgs Trilinear Coupling

We now discuss the variation of the Higgs trilinear coupling  $\lambda_{111}$  in this model fully accounting for theoretical constraints and in scenarios S1-S4. In Fig. 6 we show the values of (a)  $\lambda_{111}$  and (b)  $\lambda_{112}$  when the  $pp \rightarrow h_2 \rightarrow h_1 h_1$  rate is maximized using current LHC limits. While for most of the benchmark points,  $\lambda_{111}$  is within  $\sim 50\%$  of the SM prediction, it can be enhanced by upwards of a factor of two for  $m_2 \sim 700$  GeV. In Fig. 6(c) we show maximum and minimum allowed values of  $\lambda_{111}$  considering all theoretical and current LHC constraints, and in (d) the corresponding  $pp \rightarrow h_2 \rightarrow h_1 h_1$  rate. With current constraints, the  $\lambda_{111}$  can still be a factor 2.5 larger than the SM value. For comparison, the  $1\sigma$  and  $2\sigma$  projected bounds on  $\lambda_{111}$  at the HL-LHC are also shown [5]. The maximum allowed values of  $\lambda_{111}$  are less than the projected  $2\sigma$  bounds. A similar study was done in the  $Z_2$  symmetric real singlet model [18]. That study found larger variations in  $\lambda_{111}$ , but had weaker constraints on  $\sin \theta$  due to being conducted several years ago. The current, stronger limits on the scalar mixing angle limit how large the Higgs trilinear coupling can be.

Figure 7 shows the same results as Fig. 6, but for the future collider scenarios HL-LHC (S2), HL-LHC+FCCee (S3), and HL-LHC+ILC500 (S4). For comparison, the  $1\sigma$  and  $2\sigma$  projected bounds on  $\lambda_{111}$  at the HL-LHC are also shown [5]. Similarly to the current LHC results, when the  $h_2 \rightarrow h_1 h_1$  rate is maximized,  $\lambda_{111}$  can be up to a factor of two larger than the SM prediction, within the allowed projected  $2\sigma$  limit on  $\lambda_{111}$  at the HL-LHC. In the future lepton collider scenarios, the maximum allowed  $\lambda_{111}$  is always within the  $1\sigma$  bounds at the HL-LHC. This is due to the strong constraints on  $|\sin \theta|$  and the perturbative unitarity bound on  $a_2$  [see Eqs. (10,20)]. If the perturbative unitarity upper limit on  $a_2$  is relaxed, the variation on  $\lambda_{111}$  can be larger.

The maximum allowed  $\lambda_{111}$  is up to a factor of three larger than the SM prediction in

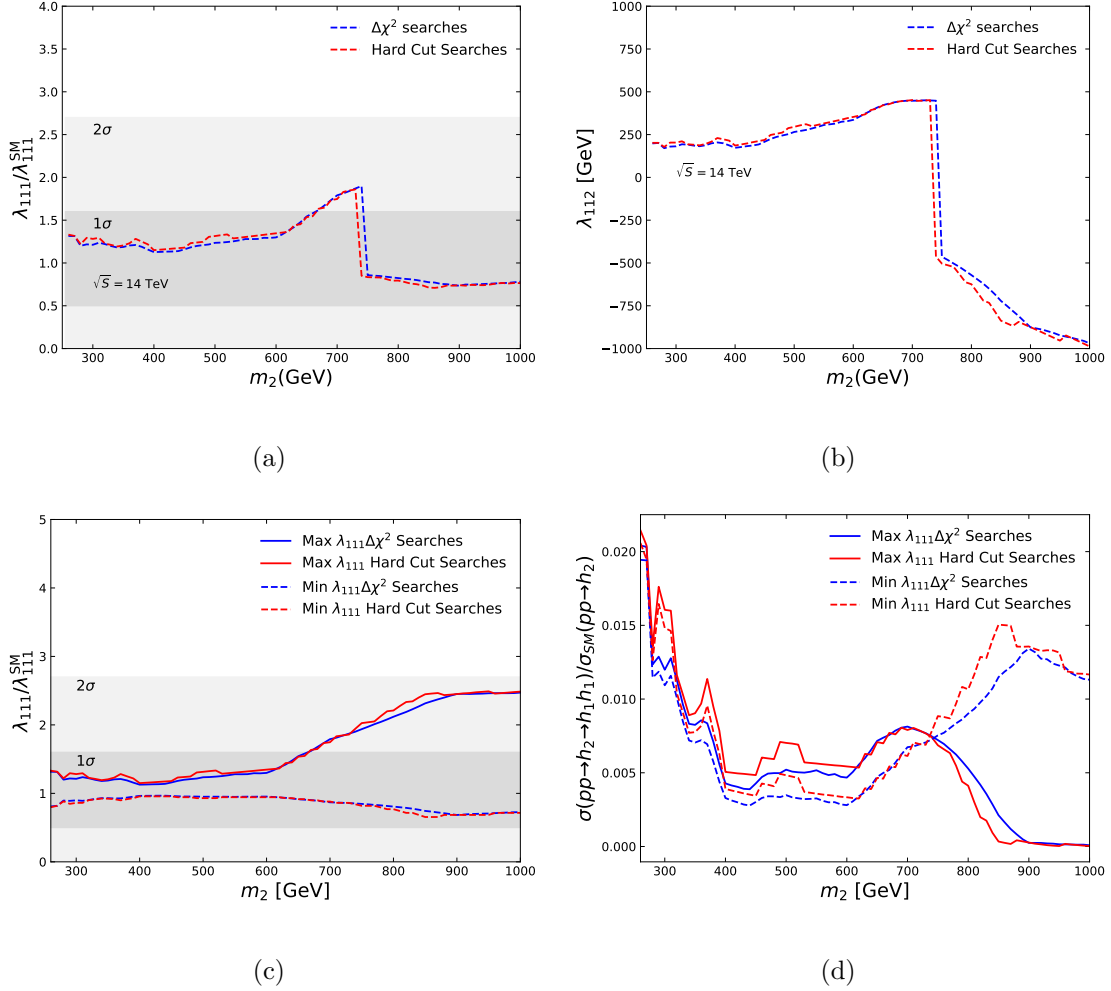


FIG. 6: The values of (a)  $\lambda_{111}$  normalized to the SM prediction  $\lambda_{111}^{\text{SM}}$  and (b)  $\lambda_{112}$  corresponding to the maximum di-Higgs rate. The (solid) maximum and (dashed) minimum allowed  $\lambda_{111}$  are shown in (c), and the corresponding  $pp \rightarrow h_2 \rightarrow h_1 h_1$  rates in (d). All results are presented for current LHC constraints using the (blue)  $\Delta\chi^2$  and (red) hard cut combinations of Higgs precision scalar searches. In (a,c) the  $1\sigma$  and  $2\sigma$  projected bounds on  $\lambda_{111}$  at the HL-LHC [5] are shown in dark and light grey shaded regions, respectively.

scenario S2. This maximum occurs for  $m_2 \sim 1.5\text{--}3.5$  TeV, which may be difficult to discover through resonant projection of  $h_2$  at the HL-LHC due to suppressed production rates at high masses.

There are some interesting behaviors when  $\lambda_{111}$  is maximized or minimized. In particular, when  $\lambda_{111}$  is maximized there are certain resonance masses for which  $\lambda_{112}$  and the  $pp \rightarrow h_2 \rightarrow h_1 h_1$  rate becomes nearly zero. To understand these, we take the small mixing angle limits



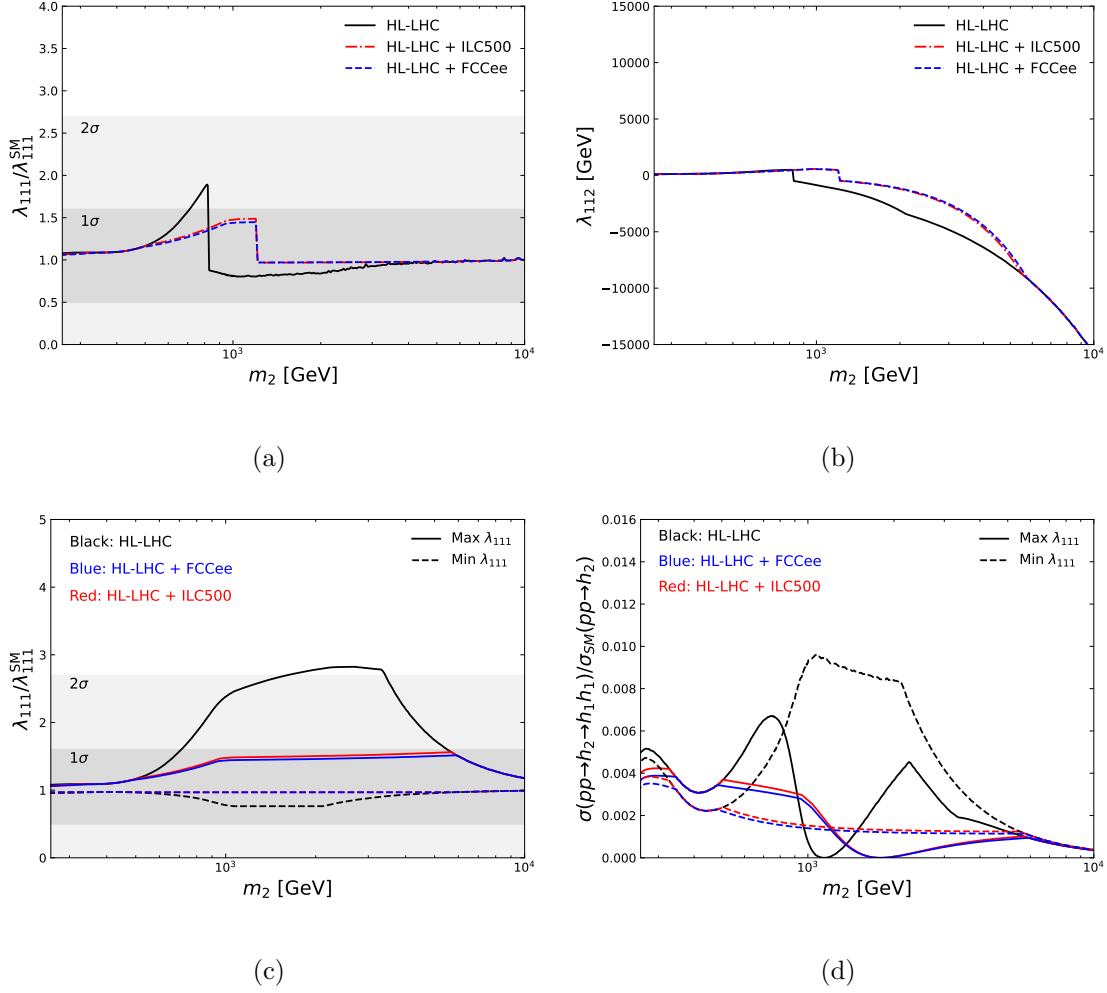


FIG. 7: The values of (a)  $\lambda_{111}$  normalized to the SM prediction  $\lambda_{111}^{\text{SM}}$  and (b)  $\lambda_{112}$  corresponding to the maximum di-Higgs rate. The (solid) maximum and (dashed) minimum allowed  $\lambda_{111}$  are shown in (c), and the corresponding  $pp \rightarrow h_2 \rightarrow h_1 h_1$  rates in (d). All results are presented for scenarios (black) S2, (blue) S3, and (red) S4. In (a,c) the  $1\sigma$  and  $2\sigma$  projected bounds on  $\lambda_{111}$  at the HL-LHC [5] are shown in dark and light grey shaded regions, respectively.

of the Higgs trilinear coupling and  $\lambda_{112}$  in Eq. (10,11):

$$\lambda_{111} = \lambda_{111}^{\text{SM}} \left[ 1 + \left( a_2 \frac{v_{\text{EW}}^2}{m_1^2} - \frac{3}{2} \right) \sin^2 \theta \right] + \mathcal{O}(\sin^3 \theta), \quad (31)$$

$$\lambda_{112} = \left( 2 a_2 v_{\text{EW}} - \frac{2 m_1^2 + m_2^2}{v_{\text{EW}}} \right) \sin \theta + 2 b_3 \sin^2 \theta + \mathcal{O}(\sin^3 \theta), \quad (32)$$

where  $\lambda_{111}^{\text{SM}}$  is the SM prediction. The expansion for the Higgs trilinear coupling  $\lambda_{111}$  shows that it is maximized or minimized by choosing the largest allowed  $|\sin \theta|$  and then maximiz-

ing or minimizing  $a_2$ . From Eqs. (7,20), the numerical bounds on  $a_2$  are

$$-1.5 + \mathcal{O}(\sin^2 \theta) \leq a_2 \leq 25. \quad (33)$$

Since the magnitude of the lower bound  $a_2$  is much smaller than the upper bound, the minimum of  $\lambda_{111}$  is near the SM value while the maximum can still have fairly large enhancements. However, the perturbative unitarity upper bound on  $a_2$  is not always saturated. For smaller masses, global minimization places stronger bounds on  $a_2$  than perturbative unitarity [13]. As  $m_2$  increases, the bounds on  $a_2$  relax until they reach the perturbative unitarity bound. Hence, the maximum  $\lambda_{111}$  increases with  $m_2$  and then flattens out when the allowed  $a_2$  saturates  $8\pi$  and  $\sin \theta$  reaches the precision Higgs limits. Then, in the multi-TeV range the narrow width constraints on  $\sin \theta$  cause the maximum  $\lambda_{111}$  to decrease.

Another interesting behavior is that when  $\lambda_{111}$  is maximized, there are resonance masses at which  $\lambda_{112}$  is very small. From Eq. (31) the maximum  $\lambda_{111}$  has no dependence on  $m_2$  except indirectly through  $a_2$  and  $\sin \theta$ . Once the model parameters are fixed, there is a mass for which  $\lambda_{112}$  is small and nearly zero:

$$m_2 = \sqrt{2(a_2 v_{EW}^2 - m_1^2)} \left( 1 + \frac{1}{2} \frac{b_3 v_{EW}}{a_2 v_{EW}^2 - m_1^2} \sin \theta \right) + \mathcal{O}(\sin^2 \theta). \quad (34)$$

Assuming the perturbative unitarity constraint is saturated, then numerical value of  $m_2$  is

$$m_2 \approx 1.7 \text{ TeV} + 0.03 \text{ TeV} \frac{b_3}{v_{EW}} \sin \theta. \quad (35)$$

This is precisely where the very small  $pp \rightarrow h_2 \rightarrow h_1 h_1$  rate occurs when maximizing  $\lambda_{111}$  in the HL-LHC+FCCee and HL-LHC+ILC500 scenarios. Hence, measurements of  $\lambda_{111}$  and searches for the  $h_2 \rightarrow h_1 h_1$  resonance can provide complementary information about the parameter space of the real singlet scalar model.

## V. SUMMARY AND CONCLUSIONS

In this paper we studied the di-Higgs rate in the simplest extension of the SM: the real singlet model with no additional symmetry. This model is interesting in that it can generate resonant production of di-Higgs and change the Higgs trilinear coupling away from SM predictions. We considered various scenarios for current and future colliders:

- S1: Current LHC constraints from precision Higgs measurements and scalar searches [44].

- S2: Projections for Higgs measurements and scalar searches at the HL-LHC [2, 3].
- S3: Projections for Higgs measurements and scalar searches at the HL-LHC and a future circular  $e^-e^+$  collider such as the CEPC or FCC-ee (HL-LHC+FCCee) [2, 3]
- S4: Projections for Higgs measurements and scalar searches at the HL-LHC and a future linear  $e^-e^+$  collider such as the 500 GeV ILC (HL-LHC+ILC500) [2, 3]

Scenarios S1 is an update on previous results in Ref. [1], while scenarios S2-S4 go beyond and provide benchmarks for future high energy colliders for resonance masses up to 10 TeV.

Considering these scenarios, the maximum allowed resonant di-Higgs  $pp \rightarrow h_2 \rightarrow h_1 h_1$  rate was found. All theoretical constraints were considered, and we presented extensive discussions on the interplay between various constraints, the maximum resonant rate, and the corresponding scalar mixing angle and  $h_2 \rightarrow h_1 h_1$  branching ratio. In scenarios S2-S4, the results are presented such that they are widely applicable for many future high energy collider possibilities. For scenario S1, resonant di-Higgs production in this model can still be up to an order of magnitude larger than the SM di-Higgs rate.

We also studied how large deviations in the SM-like Higgs trilinear coupling  $h_1 - h_1 - h_1$  can be in this model. Here we also provided a discussion on the interplay of various model constraints, the behavior of the maximum and minimum of  $\lambda_{111}$ , and the resonant  $pp \rightarrow h_2 \rightarrow h_1 h_1$  rates. Boundedness and perturbative unitarity constraints force the minimum Higgs trilinear to be near the SM value while there can still be fairly large enhancements to  $\lambda_{111}$ . Additionally, when  $\lambda_{111}$  is maximized there is a value of the resonance mass for which the rate of  $pp \rightarrow h_2 \rightarrow h_1 h_1$  is quite small, showing that resonant searches and measurements of  $\lambda_{111}$  provide complementary information on the real singlet model parameter space. We gave an analytical understanding of these behaviors.

The trilinear Higgs coupling can be up to a factor of 2.5 larger than the SM prediction in scenario S1 with resonance masses below 1 TeV, within the  $2\sigma$  projected bounds of the HL-LHC. In scenario S2 the trilinear Higgs couplings can be up a factor 3 larger than the SM prediction, just at the  $2\sigma$  sensitivity threshold for the HL-LHC. In the future lepton collider scenarios, the allowed ranges of  $\lambda_{111}$  are within 50% of the SM prediction and within the  $1\sigma$  HL-LHC constraints on  $\lambda_{111}$ . Of particular interest, the maximum value of  $\lambda_{111}$  in the HL-LHC scenario (S2) is at or above the HL-LHC projected constraints on the Higgs trilinear coupling for new scalar mass in 1.5 – 3.5 TeV range. Such high masses may be

difficult to discover through resonant production due to suppressed production rates. Hence, measurements of the Higgs trilinear coupling through non-resonant di-Higgs production and resonant di-Higgs searches at the HL-LHC will provide sensitivity to complementary regions of parameter space.

## Acknowledgements

JS, IML, and MASA are supported in part by the United States Department of Energy grant number DE-SC0017988. MS is also supported by the United States Department of Energy under Grant Contract DE-SC0012704. Digital data for the plots and benchmark points have been uploaded with the arXiv version of this paper.

- 
- [1] I. M. Lewis and M. Sullivan, *Benchmarks for Double Higgs Production in the Singlet Extended Standard Model at the LHC*, *Phys. Rev. D* **96** no. 3, (2017) 035037, [arXiv:1701.08774 \[hep-ph\]](#).
  - [2] S. Dawson *et al.*, *Report of the Topical Group on Higgs Physics for Snowmass 2021: The Case for Precision Higgs Physics*, in *Snowmass 2021*. 9, 2022. [arXiv:2209.07510 \[hep-ph\]](#).
  - [3] R. K. Ellis *et al.*, *Physics Briefing Book: Input for the European Strategy for Particle Physics Update 2020*, [arXiv:1910.11775 \[hep-ex\]](#).
  - [4] J. Alison *et al.*, *Higgs boson potential at colliders: Status and perspectives*, *Rev. Phys.* **5** (2020) 100045, [arXiv:1910.00012 \[hep-ph\]](#).
  - [5] **ATLAS** Collaboration, *Projected sensitivity of Higgs boson pair production combining the  $b\bar{b}\gamma\gamma$  and  $b\bar{b}\tau^+\tau^-$  final states with the ATLAS detector at the HL-LHC*, Tech. Rep. ATL-PHYS-PUB-2022-005, CERN, Geneva, 2022.
  - [6] V. Silveira and A. Zee, *SCALAR PHANTOMS*, *Phys. Lett. B* **161** (1985) 136–140.
  - [7] D. O’Connell, M. J. Ramsey-Musolf, and M. B. Wise, *Minimal Extension of the Standard Model Scalar Sector*, *Phys. Rev. D* **75** (2007) 037701, [arXiv:hep-ph/0611014](#).
  - [8] V. Barger, P. Langacker, M. McCaskey, M. J. Ramsey-Musolf, and G. Shaughnessy, *LHC Phenomenology of an Extended Standard Model with a Real Scalar Singlet*, *Phys. Rev. D* **77** (2008) 035005, [arXiv:0706.4311 \[hep-ph\]](#).

- [9] M. Bowen, Y. Cui, and J. D. Wells, *Narrow trans-TeV Higgs bosons and  $H \rightarrow hh$  decays: Two LHC search paths for a hidden sector Higgs boson*, *JHEP* **03** (2007) 036, [arXiv:hep-ph/0701035](#).
- [10] J. M. No and M. Ramsey-Musolf, *Probing the Higgs Portal at the LHC Through Resonant di-Higgs Production*, *Phys. Rev. D* **89** no. 9, (2014) 095031, [arXiv:1310.6035 \[hep-ph\]](#).
- [11] G. M. Pruna and T. Robens, *Higgs singlet extension parameter space in the light of the LHC discovery*, *Phys. Rev. D* **88** no. 11, (2013) 115012, [arXiv:1303.1150 \[hep-ph\]](#).
- [12] S. Profumo, M. J. Ramsey-Musolf, C. L. Wainwright, and P. Winslow, *Singlet-catalyzed electroweak phase transitions and precision Higgs boson studies*, *Phys. Rev. D* **91** no. 3, (2015) 035018, [arXiv:1407.5342 \[hep-ph\]](#).
- [13] C.-Y. Chen, S. Dawson, and I. M. Lewis, *Exploring resonant di-Higgs boson production in the Higgs singlet model*, *Phys. Rev. D* **91** no. 3, (2015) 035015, [arXiv:1410.5488 \[hep-ph\]](#).
- [14] S. Dawson and I. M. Lewis, *NLO corrections to double Higgs boson production in the Higgs singlet model*, *Phys. Rev. D* **92** no. 9, (2015) 094023, [arXiv:1508.05397 \[hep-ph\]](#).
- [15] D. Buttazzo, F. Sala, and A. Tesi, *Singlet-like Higgs bosons at present and future colliders*, *JHEP* **11** (2015) 158, [arXiv:1505.05488 \[hep-ph\]](#).
- [16] T. Robens and T. Stefaniak, *Status of the Higgs Singlet Extension of the Standard Model after LHC Run 1*, *Eur. Phys. J. C* **75** (2015) 104, [arXiv:1501.02234 \[hep-ph\]](#).
- [17] T. Robens and T. Stefaniak, *LHC Benchmark Scenarios for the Real Higgs Singlet Extension of the Standard Model*, *Eur. Phys. J. C* **76** no. 5, (2016) 268, [arXiv:1601.07880 \[hep-ph\]](#).
- [18] L. Di Luzio, R. Gröber, and M. Spannowsky, *Maxi-sizing the trilinear Higgs self-coupling: how large could it be?*, *Eur. Phys. J. C* **77** no. 11, (2017) 788, [arXiv:1704.02311 \[hep-ph\]](#).
- [19] T. Huang, J. M. No, L. Pernié, M. Ramsey-Musolf, A. Safonov, M. Spannowsky, and P. Winslow, *Resonant di-Higgs boson production in the  $b\bar{b}WW$  channel: Probing the electroweak phase transition at the LHC*, *Phys. Rev. D* **96** no. 3, (2017) 035007, [arXiv:1701.04442 \[hep-ph\]](#).
- [20] S. Dawson, C. Englert, and T. Plehn, *Higgs Physics: It ain't over till it's over*, *Phys. Rept.* **816** (2019) 1–85, [arXiv:1808.01324 \[hep-ph\]](#).
- [21] H.-L. Li, M. Ramsey-Musolf, and S. Willocq, *Probing a scalar singlet-catalyzed electroweak phase transition with resonant di-Higgs boson production in the  $4b$  channel*, *Phys. Rev. D* **100** no. 7, (2019) 075035, [arXiv:1906.05289 \[hep-ph\]](#).

- [22] A. Alves, D. Gonçalves, T. Ghosh, H.-K. Guo, and K. Sinha, *Di-Higgs Blind Spots in Gravitational Wave Signals*, *Phys. Lett. B* **818** (2021) 136377, [arXiv:2007.15654 \[hep-ph\]](#).
- [23] S. Dawson, S. Homiller, and S. D. Lane, *Putting standard model EFT fits to work*, *Phys. Rev. D* **102** no. 5, (2020) 055012, [arXiv:2007.01296 \[hep-ph\]](#).
- [24] S. Adhikari, I. M. Lewis, and M. Sullivan, *Beyond the Standard Model effective field theory: The singlet extended Standard Model*, *Phys. Rev. D* **103** no. 7, (2021) 075027, [arXiv:2003.10449 \[hep-ph\]](#).
- [25] T. Cohen, N. Craig, X. Lu, and D. Sutherland, *Is SMEFT Enough?*, *JHEP* **03** (2021) 237, [arXiv:2008.08597 \[hep-ph\]](#).
- [26] S. Dawson, P. P. Giardino, and S. Homiller, *Uncovering the High Scale Higgs Singlet Model*, *Phys. Rev. D* **103** no. 7, (2021) 075016, [arXiv:2102.02823 \[hep-ph\]](#).
- [27] A. Hammad, S. Moretti, and M. Nojiri, *Multi-scale cross-attention transformer encoder for event classification*, *JHEP* **03** (2024) 144, [arXiv:2401.00452 \[hep-ph\]](#).
- [28] F. Feuerstake, E. Fuchs, T. Robens, and D. Winterbottom, *Interference effects in resonant di-Higgs production at the LHC in the Higgs singlet extension*, [arXiv:2409.06651 \[hep-ph\]](#).
- [29] S. Profumo, M. J. Ramsey-Musolf, and G. Shaughnessy, *Singlet Higgs phenomenology and the electroweak phase transition*, *JHEP* **08** (2007) 010, [arXiv:0705.2425 \[hep-ph\]](#).
- [30] A. V. Kotwal, M. J. Ramsey-Musolf, J. M. No, and P. Winslow, *Singlet-catalyzed electroweak phase transitions in the 100 TeV frontier*, *Phys. Rev. D* **94** no. 3, (2016) 035022, [arXiv:1605.06123 \[hep-ph\]](#).
- [31] A. Papaefstathiou and G. White, *The electro-weak phase transition at colliders: confronting theoretical uncertainties and complementary channels*, *JHEP* **05** (2021) 099, [arXiv:2010.00597 \[hep-ph\]](#).
- [32] A. Papaefstathiou and G. White, *The Electro-Weak Phase Transition at Colliders: Discovery Post-Mortem*, *JHEP* **02** (2022) 185, [arXiv:2108.11394 \[hep-ph\]](#).
- [33] J. R. Espinosa, T. Konstandin, and F. Riva, *Strong Electroweak Phase Transitions in the Standard Model with a Singlet*, *Nucl. Phys. B* **854** (2012) 592–630, [arXiv:1107.5441 \[hep-ph\]](#).
- [34] D. Curtin, P. Meade, and C.-T. Yu, *Testing Electroweak Baryogenesis with Future Colliders*, *JHEP* **11** (2014) 127, [arXiv:1409.0005 \[hep-ph\]](#).
- [35] V. Vaskonen, *Electroweak baryogenesis and gravitational waves from a real scalar singlet*,

- Phys. Rev. D* **95** no. 12, (2017) 123515, [arXiv:1611.02073 \[hep-ph\]](#).
- [36] P. Huang, A. J. Long, and L.-T. Wang, *Probing the Electroweak Phase Transition with Higgs Factories and Gravitational Waves*, *Phys. Rev. D* **94** no. 7, (2016) 075008, [arXiv:1608.06619 \[hep-ph\]](#).
  - [37] A. Beniwal, M. Lewicki, J. D. Wells, M. White, and A. G. Williams, *Gravitational wave, collider and dark matter signals from a scalar singlet electroweak baryogenesis*, *JHEP* **08** (2017) 108, [arXiv:1702.06124 \[hep-ph\]](#).
  - [38] G. Kurup and M. Perelstein, *Dynamics of Electroweak Phase Transition In Singlet-Scalar Extension of the Standard Model*, *Phys. Rev. D* **96** no. 1, (2017) 015036, [arXiv:1704.03381 \[hep-ph\]](#).
  - [39] C.-Y. Chen, J. Kozaczuk, and I. M. Lewis, *Non-resonant Collider Signatures of a Singlet-Driven Electroweak Phase Transition*, *JHEP* **08** (2017) 096, [arXiv:1704.05844 \[hep-ph\]](#).
  - [40] A. Beniwal, M. Lewicki, M. White, and A. G. Williams, *Gravitational waves and electroweak baryogenesis in a global study of the extended scalar singlet model*, *JHEP* **02** (2019) 183, [arXiv:1810.02380 \[hep-ph\]](#).
  - [41] K. Ghorbani and P. H. Ghorbani, *Strongly First-Order Phase Transition in Real Singlet Scalar Dark Matter Model*, *J. Phys. G* **47** no. 1, (2020) 015201, [arXiv:1804.05798 \[hep-ph\]](#).
  - [42] A. Mazumdar and G. White, *Review of cosmic phase transitions: their significance and experimental signatures*, *Rept. Prog. Phys.* **82** no. 7, (2019) 076901, [arXiv:1811.01948 \[hep-ph\]](#).
  - [43] P. Ghorbani, *Vacuum structure and electroweak phase transition in singlet scalar dark matter*, *Phys. Dark Univ.* **33** (2021) 100861, [arXiv:2010.15708 \[hep-ph\]](#).
  - [44] S. D. Lane, I. M. Lewis, and M. Sullivan, *Resonant Multi-Scalar Production in the Generic Complex Singlet Model in the Multi-TeV Region*, [arXiv:2403.18003 \[hep-ph\]](#).
  - [45] *The International Linear Collider Technical Design Report - Volume 1: Executive Summary*, [arXiv:1306.6327 \[physics.acc-ph\]](#).
  - [46] **ILC** Collaboration, *The International Linear Collider Technical Design Report - Volume 2: Physics*, [arXiv:1306.6352 \[hep-ph\]](#).
  - [47] *The International Linear Collider Technical Design Report - Volume 3.I: Accelerator \& in*

- the Technical Design Phase*, [arXiv:1306.6353](#) [[physics.acc-ph](#)].
- [48] **CEPC Study Group** Collaboration, *CEPC Conceptual Design Report: Volume 1 - Accelerator*, [arXiv:1809.00285](#) [[physics.acc-ph](#)].
  - [49] M. Dong *et al.*, , **CEPC Study Group** Collaboration, *CEPC Conceptual Design Report: Volume 2 - Physics & Detector*, [arXiv:1811.10545](#) [[hep-ex](#)].
  - [50] A. Abada *et al.*, , **FCC** Collaboration, *FCC-ee: The Lepton Collider: Future Circular Collider Conceptual Design Report Volume 2*, *Eur. Phys. J. ST* **228** no. 2, (2019) 261–623.
  - [51] J. Tang *et al.*, *Concept for a Future Super Proton-Proton Collider*, [arXiv:1507.03224](#) [[physics.acc-ph](#)].
  - [52] M. Ahmad *et al.*, *CEPC-SPPC Preliminary Conceptual Design Report. 1. Physics and Detector*, Tech. Rep. IHEP-CEPC-DR-2015-01, IHEP-TH-2015-01, IHEP-EP-2015-01, 3, 2015.
  - [53] A. Abada *et al.*, , **FCC** Collaboration, *FCC-hh: The Hadron Collider: Future Circular Collider Conceptual Design Report Volume 3*, *Eur. Phys. J. ST* **228** no. 4, (2019) 755–1107.
  - [54] R. B. Palmer *et al.*, *Muon colliders*, *AIP Conf. Proc.* **372** no. 1, (1996) 3–30, [arXiv:acc-physics/9602001](#).
  - [55] J. P. Delahaye, M. Diemoz, K. Long, B. Mansoulié, N. Pastrone, L. Rivkin, D. Schulte, A. Skrinsky, and A. Wulzer, *Muon Colliders*, [arXiv:1901.06150](#) [[physics.acc-ph](#)].
  - [56] K. M. Black *et al.*, *Muon Collider Forum report*, *JINST* **19** no. 02, (2024) T02015, [arXiv:2209.01318](#) [[hep-ex](#)].
  - [57] J. de Blas *et al.*, , **Muon Collider** Collaboration, *The physics case of a 3 TeV muon collider stage*, [arXiv:2203.07261](#) [[hep-ph](#)].
  - [58] S. Navas *et al.*, , **Particle Data Group** Collaboration, *Review of particle physics*, *Phys. Rev. D* **110** no. 3, (2024) 030001.
  - [59] A. Schuessler and D. Zeppenfeld, *Unitarity constraints on MSSM trilinear couplings*, in *15th International Conference on Supersymmetry and the Unification of Fundamental Interactions (SUSY07)*, pp. 236–239. 10, 2007. [arXiv:0710.5175](#) [[hep-ph](#)].
  - [60] P. Bechtle, O. Brein, S. Heinemeyer, G. Weiglein, and K. E. Williams, *HiggsBounds: Confronting Arbitrary Higgs Sectors with Exclusion Bounds from LEP and the Tevatron*, *Comput. Phys. Commun.* **181** (2010) 138–167, [arXiv:0811.4169](#) [[hep-ph](#)].
  - [61] H. Bahl, T. Biekötter, S. Heinemeyer, C. Li, S. Paasch, G. Weiglein, and J. Wittbrodt,



*HiggsTools: BSM scalar phenomenology with new versions of HiggsBounds and HiggsSignals,*  
*Comput. Phys. Commun.* **291** (2023) 108803, [arXiv:2210.09332 \[hep-ph\]](#).